VOL. 19, NO. 8, APRIL 2024 ISSN 1819-6608
ARPN Journal of Engineering and Applied Sciences

www.arpnjournals.com

CLASSIFICATION AND DETECTION OF CHANGES IN LAND USE AND LAND COVER USING SATELLITE IMAGES AND GIS- NEAR SUEZ CANAL AREA

Mayada R. Attia[1,3], Ibrahim F. Shaker[1], Alaa Al Din I. Awad[1] and A. M. Abdel-Wahab[2]
[1]Department of Civil Engineering, Ain Shams University, Faculty of Engineering, Cairo, Egypt
[2]Department of Civil Engineering, Engineering and Renewable Energy Research Institute, National Research Centre, Cairo, Egypt
[3]Department of Civil Engineering, Demonstrator, Suez Canal University, Faculty of Engineering, Ismailia, Egypt
E-Mail: mayadareda@eng.suez.edu.eg

ABSTRACT

Egypt has developed significantly in the vicinity of the Suez Canal and its surrounding towns over the last ten years. Utilizing satellite pictures to identify land use and cover types from thematic maps remains difficult. Select the optimal strategy for successful satellite image classification across various applications. Enhancing classification accuracy requires the most effective algorithm. The effectiveness of a change detection system has not been tested in the community of Abu SUWEIR, located near the Suez Canal region in Ismailia City, Egypt. This project analyzes seven classification algorithms with the use of remotely sensed Planet Scope multispectral pictures to evaluate and monitor changes in land cover in ABU SUWEIR Village from 2016 to 2022. The post-January 25, 2011 revolution period in Egypt saw a transition from anarchy to the commencement of progress and improvement. This analysis demonstrates that the ANN classifier achieved an overall accuracy of 77.33% in 2016 and 72.00% in 2022, with corresponding KAPPA coefficients of 0.66 and 0.58 for each year. Agriculture was the most common land use type according to the ANN categorization, making up over 60.48% of the study area in 2016 and 53.89% in 2022. Bare terrain is the second most common landcover type, accounting for 30.31% in 2022 and 25.91% in 2016. On the contrary, urbanized regions, accounting for 13.61% in 2016 and 15.80% in 2022, are the least categorized.

Keywords: planetscope imagery, image classification algorithms, change detection, encroachment.

Manuscript Received 5 March 2024; Revised 17 May 2024; Published 30 June 2024

1. INTRODUCTION

Following the January 25, 2011 revolution in Egypt, there was significant encroachment on agricultural fields and unplanned building between 2011 and 2014. Subsequently, upon the restoration of state authority and order, the development plan was initiated to establish the new republic. The areas that have changed include the Suez Canal axis and the canal cities where they are situated. The research area was selected due to the absence of prior similar studies to assess the changes in land use within this region.

Every Egyptian development strategy and sustainable development plan prioritizes agriculture. Land is a limited resource that can only be partially restored after a change [1], and over 70% of the world's ice-free land area is impacted by human activity [2]. Consequently, the competition for land use is growing as a result of the world's population growth and economic globalization [3, 4]. Urbanization, which boosts modernity, industry, and globalization, is good, but urban settlements on agricultural land may be devastating [5, 6]. It's necessary to thoroughly analyze how land use changes may influence the environment. Land cover change data from dynamical and multitemporal remote sensing may be best for assessing and analyzing these changes [7]. Remote sensing (RS) satellites and GIS are used to monitor urban expansion and deterioration in rural regions. RS is used to identify and characterize land cover changes. RS has been used in several growth investigations [8, 9, 10, 11]. Timely, high- and medium-resolution remote sensing satellite photos can visually and statistically monitor urban expansion and land cover change [12]. GIS simplifies urban planning by showing, storing, and analyzing digital maps of land cover changes. The quantitative distribution of land cover classes in change detection makes it a vital RS approach for analyzing land cover changes [13]. Because RS and GIS offer a variety of possibilities for environmental preservation, decision-makers commonly use them to aid in planning, improvement, and conservation [14, 15]. Additionally, it offers helpful data for a variety of applications in environmental preservation, sustainable land management, and socioeconomic transformation [16, 17]. The research tested numerous image classification algorithms on a typical Egyptian rural hamlet. Satellite images from six years before and after ABU SUWEIR's commissioning were used. ENVI, and ArcGIS, two popular remote sensing image processing software packages provided the algorithms. The goal is to analyze a multitemporal satellite image of a region that meets the definition of a typic region using seven classifiers-Maximum likelihood (ML), Minimum Distance (MD), Mahalanobis Distance (MhD), Spectral Angle Mapper (SAM), Artificial Neural Network (ANN), K-mean, Iterative Self-Organizing Data Analysis Technique Algorithm (ISO-DATA) and detect the change occurs to the agriculture lands of ABU SUWIER due to Encroachment on agriculture lands. No satisfactory studies

ARPN Journal of Engineering and Applied Sciences

have been conducted in Egyptian villages. This research is needed now.

2. STUDY AREA

ABU SUWEIR is an Ismailia governorate division. Geographically the governorate covers 5067 km^2. ABU SUWEIR is located 101 km northeast of Cairo between 30° 10' N and 31° 13' N and 32° 48' E and 32° 50' E as shown in Figure-1.

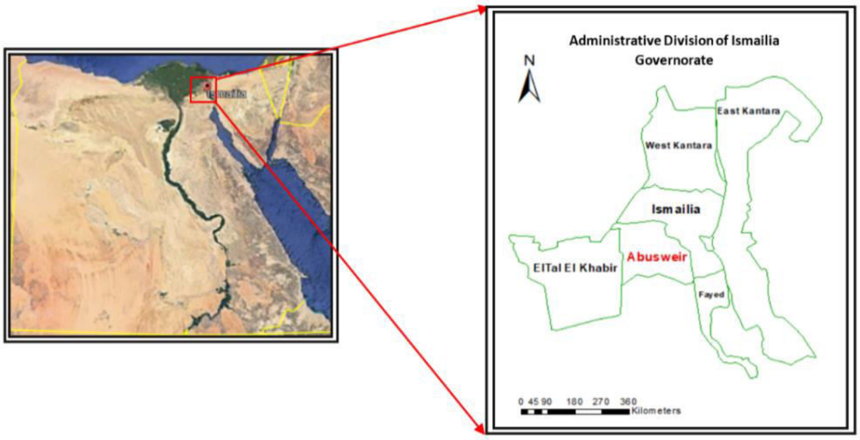

Figure-1. Geographic location of the study area (Source: Author, 2023).

3. METHODS

3.1 Data Source (Satellite Images)

Planet Labs (https://www.planet.com/) provided two Planet Scope images of the study area to the Egyptian Ministry of Planning and Economic Development and National Spatial Data Infrastructure (https://mped.gov.eg/) to examine six years of land use and land cover change. Table-1 shows the four bands of PlanetScope pictures with a spatial resolution of 3m, and Table 2 lists the data utilized in this study.

Table-1. Spectral bands description of Planet Scope sensor.

Bands	Range of wavelength (nanometers)
Band 1 - Blue	455-515
Band 2 - Green	500-590
Band 3 - Red	590-670
Band 4 - Near Infrared (NIR)	780-860

Table-2. Details of acquired satellite images.

	Image-1	Image-2
Acquisition date	**2016**	**2022**
Spacecraft & sensor id	Planet Scope “PS2”	Planet Scope “PS2”
Spatial resolution	3m	3m
Projection	UTM, Zone 36 N	UTM, Zone 36 N

3.2 Data Analysis

Maps and graphs were used to represent ideas throughout the analysis. The temporal satellite dataset from 2016 to 2022 was examined one by one. The results of each satellite's data analysis “classification& change detection” were compared to assess the study's conclusions. The underlying flowchart was followed throughout the entire analysis process Figure-2.

ARPN Journal of Engineering and Applied Sciences

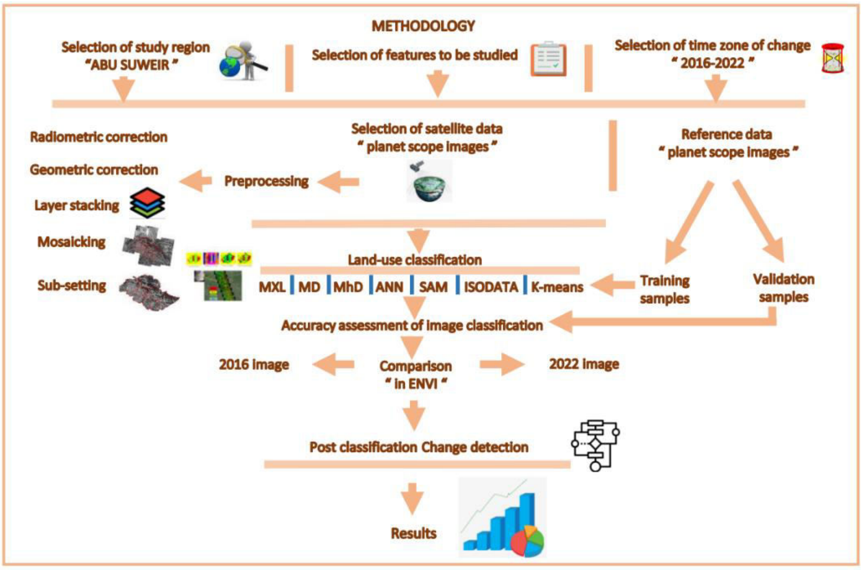

Figure-2. Methodology flowchart (Source: Author, 2023).

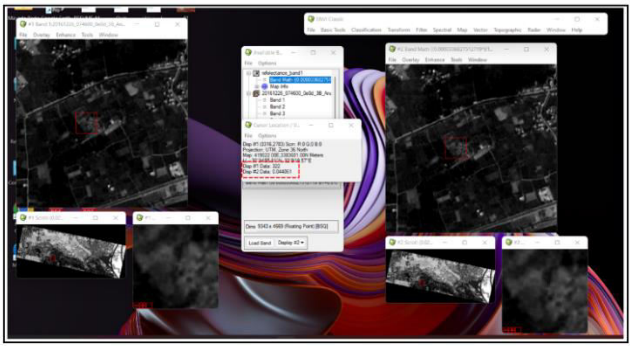

Figure-3. Radiometric calibration in ENVI for band 1 (Source: Author, 2023).

3.3 Data Preprocessing

The digital image processing of PlanetScope data between 2016 and 2022 was altered using two software programs:

a) ENVI (5.1)

b) ArcGIS (10.7)

The sceneries were radiometrically and geometrically adjusted, layers stacked, mosaicked, and sub-set for the research region.

3.3.1 Radiometric calibration

Radiometric characterization and calibration are necessary for high-quality scientific data and downstream products [18]. The main purpose was to convert digital numbers (DN) into TOP-Of-Atmosphere (TOA) units [19]. Calculations for calibrated DNs to physical units such as at-sensor radiance (TOA) have been published elsewhere [20]. Equations (1) and (2) use metadata (MTL) file rescaling coefficients to scale DN to TOA reflectance [21]:

$$\rho\lambda' = M_\rho \times Q_{cal} + A_\rho \qquad (1)$$

Where:

$\rho\lambda'$: TOA reflectance without accounting for the sun angle (Unit less), M_ρ: Multiplicative rescaling factor for a certain band, A_ρ: Band-specific reflectance additive scaling factor, Q_{cal}: Quantized and calibrated standard product pixel values (DN).

TOA reflectance with a correction for the sun angle is then:

$$\rho\lambda = \rho\lambda'/\cos(\theta_{SZ}) = \rho\lambda'/\sin(\theta_{SE}) \qquad (2)$$

Where:

$P\lambda$: TOA reflectance, θ_{SE}: Local sun elevation angle. In the metadata, there is a field for the scene center sun elevation angle in degrees, θ_{SZ}: Local solar zenith angle ($\theta_{SZ} = 90° - \theta_{SE}$).

Figure-3 offered a demonstration of radiometric calibration of a planet Scope image (for band-1 of an image, acquisition date: 26-12-2016) by methodical modeling that shows the efficient transformation of spectral radiance into TOA reflectance.

3.3.2 Geometric correction

Geometric and radiometric calibration is a crucial stage in the comparison of multi-temporal remotely sensed images [22]. For the purpose of change detection, it is also crucial to employ spatially precise multi-temporal dates. The term "geo-referencing" describes the process of locating a layer or coverage in space using a recognized coordinate system [23]. It is necessary to conduct analysis pixel-by-pixel, according to [24, 25]. The image must be registered with a root-mean-square (RMS) error of less than 0.5 pixels in order to reduce misregistration. The four images were geo-referenced to UTM Zone 36N coordinate system on the WGS 1984 datum. Images from 2016 and 2022 had pixel resolutions of 3 by 3. Geometric rectification was not required as Planet Labs (https://www.planet.com/) had correctly rectified all four photos.

3.4 Image Classification Techniques

The two main image classification methods used in this research are supervised (Maximum Likelihood, Minimum Distance, Mahalanobis Distance, Spectral Angle Mapper, and Artificial Neural Network) and unsupervised (K-means and Iterative Self-Organizing Data Analysis Technique Algorithm) classification. Based on the characteristics of the research region (ABU SUWEIR which is one of ISMAILIA's most prosperous agricultural village), a classification scheme was created to aid in the subsequent analysis of the images.

3.4.1 Supervised classification techniques

For supervised classification, representative training sample locations for each of the several land cover classes in the image are used to analyze the satellite images. The training areas in the satellite image are typical samples of the current cover type. Every pixel in the image is compared with the gathered training areas by the supervised classifiers. Training samples were categorized into two types by [26, 27] the first type was used for image classification, while the second type was utilised to assess classification accuracy. The spectral signatures are produced, according to [28], by choosing training sites based on the recognition of comparable areas in various land covers and land uses, combining the local knowledge for an appropriate selection of the regions of interest. Training areas were chosen for this study in accordance with Google Earth Pro and PlanetScope Images (Figure-4). Three classes-bare ground, urban and built-up, and agriculture-were applied to the images.

The following five supervised classifiers are used for the current study.

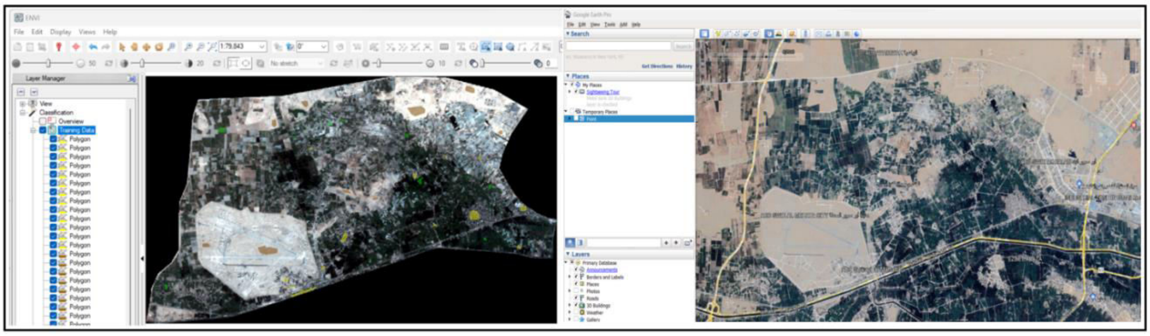

Figure-4. Identification of training areas using PlanetScope image (ENVI 5.1) and Google map pro (Source: Author, 2023).

a) Maximum Likelihood classifier (ML)

Through a combination of first-hand knowledge, interpretation of aerial photography, map analysis, and fieldwork, Maximum Likelihood detects and locates land cover categories that are already recognized [29]. It assumes that the statistics for each class in each band are normally distributed and calculates the probability that a given pixel belongs to a specific class. Unless a probability threshold is chosen, all pixels are categorized. Each pixel is assigned to the class that has the highest probability. The pixel stays unclassified if the highest likelihood is below a threshold [30]. ML classifier uses the following discriminant Equation (3) for each pixel in the image [31].

$$g_i\,(x) = \ln p(w_i) - ½ \ln|\Sigma i| - ½\,(x - m_i) t\, \Sigma i^{-1}\,(x - m_i) \tag{3}$$

Where:
i: class, x: n-dimensional data (where n is the number of bands), $p(w_i)$: Probability that class w_i occurs in the image and is assumed the same for all classes, $|\Sigma i|$: Determinant of the covariance matrix of the data in class w_i, Σi^{-1}: Its inverse matrix,
m_i: Mean vector.

b) Minimum Distance (MD)

Utilizing the MD classifier, determine the Euclidean Distance (ED) between the pixel values (xp, yp) and the mean values for the classes, and then assign the pixel to the class with the smallest ED. Additionally, a maximum distance requirement can be established, preventing pixels from being allocated to a class if they are located more than this distance from the class mean [32].

Therefore, three distances should be calculated for the three land cover classes using Distance Equation (4) as follows:

$$\mathrm{ED_A}^2 = (\mathrm{x_p} - \mathrm{x}_A)^2 + (\mathrm{y_p} - \mathrm{y}_A)^2, \mathrm{ED_B}^2 = (\mathrm{x_p} - \mathrm{x}_B)^2 + (\mathrm{y_p} - \mathrm{y}_B)^2,\ \mathrm{ED_C}^2 = (\mathrm{x_p} - \mathrm{x}_C)^2 + (\mathrm{y_p} - \mathrm{y}_C)^2 \tag{4}$$

Where:
x_p, y_p: Coordinate of unknown image, x_A, y_A: Coordinate of average class A, ED_A: Distance of class A and unknown image data, ED_B: Distance of class B and unknown image data, ED_C: Distance of class C and unknown image data.

c) Mahalanobis Distance (MhD)

The MhD employs statistics for each class and is a direction-sensitive distance classifier. Although it is similar to ML classification, it is quicker since it assumes that all class covariances are equal. Unless a distance

ARPN Journal of Engineering and Applied Sciences

criterion is specified, all pixels are assigned to the nearest region of interest (ROI) class; otherwise, some pixels may be unclassified if they do not match the threshold [19, 33]. The MhD can be calculated through equation (5):

$$d(x, m_i)^2 = (x - m_i)^T C^{-1} (x - m_i) \quad (5)$$

Where:

X: n-dimensional data (where n is the number of bands), m_i: Mean vector, C: Covariance matrix.

d) Spectral Angle Mapper (SAM)

The spectral angle mapper, which divides the spectrum domain according to the angles of vectors measured from the origin for two dimensions, is a classifier occasionally used with data of high spectral dimensionality, such as that collected by imaging spectrometers. In contrast to the more common Cartesian form, every pixel point in spectral space has both a magnitude and an angular direction when stated in polar form. The decision border is based on the most effective angular separation between the training pixels in the various classes, typically in an average sense. In terms of the SAM's applicability for high dimensional imagery, only first-order parameters are estimated, positioning it in the same category as the minimum distance technique [34, 31].

e) Artificial Neural Network (ANN)

A neural network is a computing process that uses an unstructured approach to solve problems. It consists of three layers: input, hidden, and output. In the input layer, neurons represent multispectral reflectance values, in the hidden layer, nonlinear patterns, and in the output layer, a single thematic map for each land cover class. The back-propagation algorithm is used to train the model [34].

3.4.2 Unsupervised classification techniques

In this research, there are two types of unsupervised classification were used:

a) K-means

The K-means technique divides image pixels into K-clusters iteratively, with pixels being allocated to the cluster with the closest mean in the feature space [35, 36]. The feature space, which the clustering method uses to measure similarity, is a 2-dimensional space. The maximum iterations and convergence criterion for the K-means classifier must be determined beforehand. The K-means algorithm starts by assuming random cluster centers, and then assigns pixels based on which one is closest to the center. Each cluster's standard deviation and the separation between cluster centers are computed. When the distance between two clusters is below the user-defined threshold, the clusters are only combined [21]. The Euclidean distance was described by [26] as:

$$d_E(X, Y) = \sum_{i=1}^{d} (Xi - Yi)^2 \quad (6)$$

Where:
$d_E(X,Y)$: Euclidean distance, X_i: points X in d-space dimensions, Y_i: points Y in d-space dimensions.

The number of iterations is increased until no more "k" centroids' locations may be changed, at which point the loop of iterations ends [21].

Equation (7) was used by [36] to represent the K-means method mathematically.

$$J_{k\text{-mean}} = \sum_{k=1}^{k} \sum_{j \in Sk} d^2(x_j, c_k) \quad (7)$$

Where:
k: How many clusters there are, x_j: j-pattern evaluation in respect to the centroid, $d^2(x_j,c_k)$: The separation between x_j and centroid c_k.

b) Iterative Self-Organizing Data Analysis Technique Algorithm (ISODATA) classifier

Using the shortest spectral distance between pixels and a chosen mean cluster, the ISODATA classifier iteratively allocated the pixels to the clusters. Each pixel's spectral distance to the mean of each cluster is determined, and the pixel is then allocated to the cluster with the closest mean. The determined clusters' means are updated in the subsequent iteration, and the pixels are moved and assigned to the newest clusters with the nearest means [21, 31].

3.4.3 Classification results and discussion

Five supervised & two unsupervised classifiers were conducted in the research area. The pixel count and total area were taken into consideration while calculating the area of each class for all classifiers. For the years "2016 & 2022", the allocations of each classed region (in kilometer squared and percentage) are therefore listed in Tables 3 and 4. The output thematic maps of the above classifiers are shown in Figure-5 and Figure-6.

VOL. 19, NO. 8, APRIL 2024 ISSN 1819-6608
ARPN Journal of Engineering and Applied Sciences

www.arpnjournals.com

Table-3. Land use and land cover statistics of study area for date 2016 " in kilometer square and percentage" for seven classifiers.

LU/LC	Supervised classification										Unsupervised classification			
	ML		MD		MhD		SAM		ANN		K-means		ISODATA	
	Km^2	%	Km^2	%	Km^2	%	Km^2	%	Km^2	%	Km^2	%	Km^2	%
Bare ground	16.74	23.90	22.19	31.68	20.54	29.32	33.85	48.32	18.15	25.91	30.44	43.45	23.67	33.79
Urban and built-up	16.98	24.23	20.70	29.54	25.54	36.46	11.16	15.94	9.53	13.61	9.63	13.74	9.70	13.84
Agriculture/vegetation	36.34	51.87	27.16	38.78	23.97	34.22	25.04	35.74	42.37	60.48	29.99	42.81	36.68	52.36
Total	70.05	100.00	70.05	100.00	70.05	100.00	70.05	100.00	70.05	100.00	70.05	100.00	70.05	100.00

Table-4. Land use and land cover statistics of study area for date 2022 " in kilometer square and percentage" for seven classifiers.

LU/LC	Supervised classification										Unsupervised classification			
	ML		MD		MhD		SAM		ANN		K-means		ISODATA	
	Km^2	%	Km^2	%	Km^2	%	Km^2	%	Km^2	%	Km^2	%	Km^2	%
Bare ground	17.74	25.32	22.35	31.90	15.72	22.44	22.96	32.78	21.23	30.31	32.07	45.78	31.63	45.15
Urban and built-up	14.22	20.29	19.26	27.49	13.47	19.23	13.75	19.63	11.07	15.80	29.88	42.65	26.74	38.17
Agriculture/vegetation	38.10	54.39	28.44	40.60	40.86	58.33	33.34	47.59	37.75	53.89	8.10	11.57	11.68	16.68
Total	70.05	100.00	70.05	100.00	70.05	100.00	70.05	100.00	70.05	100.00	70.05	100.00	70.05	100.00

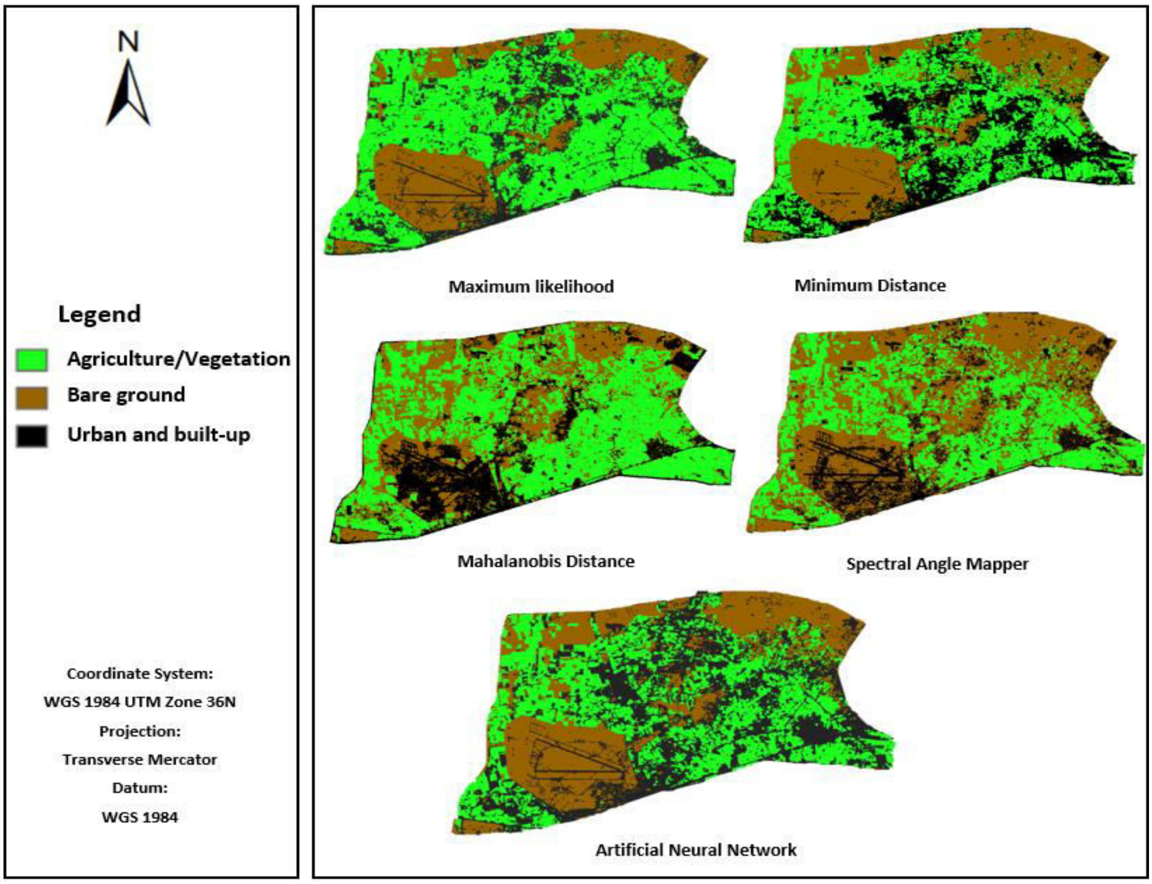

Figure-5. Classified LU/LC thematic maps of ABU SUWIER for supervised classifier (year, 2016) (Source: Author, 2023).

ARPN Journal of Engineering and Applied Sciences

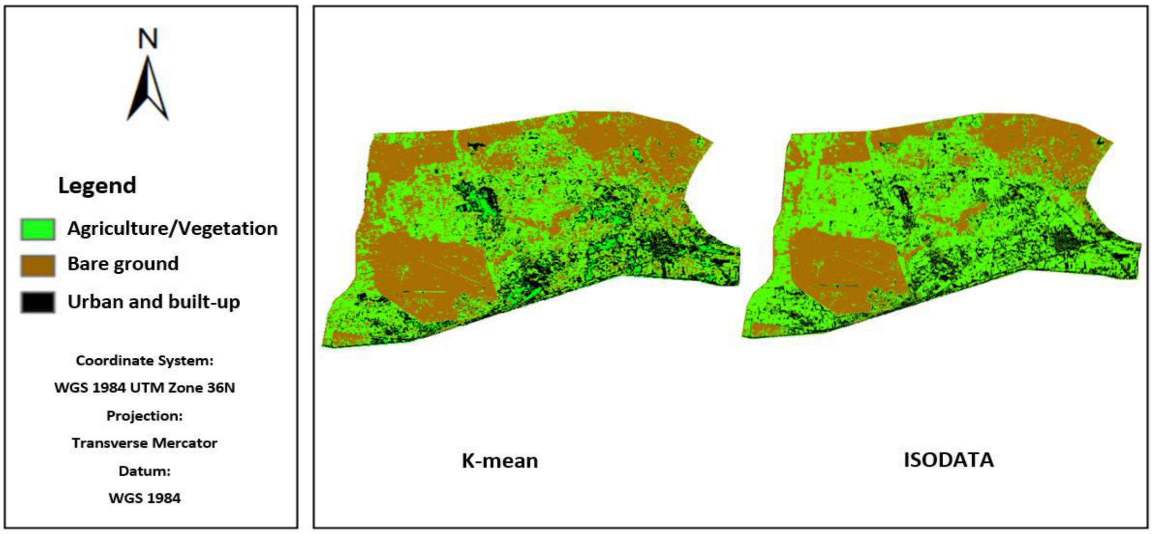

Figure-6. Classified LU/LC thematic maps of ABU SUWIER for unsupervised classifier (year, 2016) (Source: Author, 2023).

3.5 Classification Accuracy Assessment

Accuracy assessment is crucial for validating and verifying the classification results. Quantitatively evaluating how well the pixels were sampled into the appropriate land cover groups is the goal of accuracy assessment [37, 38, 10, 39]. Additionally, the primary focus for pixel selection in the accuracy assessment was on regions that were easily distinguishable on the Google Map, Google Earth Pro, and Planet Scope high resolution image. Using the equalized stratified random distribution sampling approach, the accuracy points are dispersed throughout the whole input dataset (For the purposes of the study area, each class is assigned an equal number of points) [39]. Within the classified images of this study region, 150 points (locations) were generated 50 points for each class. For the purpose of classifying the chosen points, Google Earth and Google Maps were utilised as reference sources. By employing a confusion matrix (error matrix), the data is compiled and quantified. Four distinct accuracy statistics are provided to aid in understanding how accurate the classification is: user accuracy, producer accuracy, overall accuracy, and kappa index, which is generated from the overall assessment. The overall classification accuracy was expressed by [39, 40] as presented in equation (8):

The overall accuracy = No. of correct points/total number of points (8)

The kappa coefficient was mathematically stated by [41], as seen in equation (9).

$$\text{kappa coefficient} = \frac{N\sum_{i=1}^{r} x_{ii} - \sum_{i=1}^{r}(x_{i+} * x_{+i})}{N^2 - \sum_{i=1}^{r}(x_{i+} * x_{+i})} \quad (9)$$

Where:

r : number of the error matrix's rows and columns
N : total quantity of observations
$x$ii : the observation in column i and row i
x_{i+} : total amount of pixels in row i
x_{+i} : total amount of pixels in column i

While a value near 0 indicates that the agreement is no better than would be predicted by chance, a Kappa coefficient equal to one indicates complete agreement. The classification of the Kappa statistic, which is replicated in Table-5, is based on the widely cited work of [42].

Table-5. Standards for evaluating Kappa statistics [42].

S. No	Kappa statistics	Strength of agreement
1	<0.00	Poor
2	0.00 - 0.20	Slight
3	0.21 - 0.40	Fair
4	0.41 - 0.60	Moderate
5	0.61 - 0.80	Substantial
6	0.81 - 1.00	Almost perfect

ISSN 1819-6608
ARPN Journal of Engineering and Applied Sciences

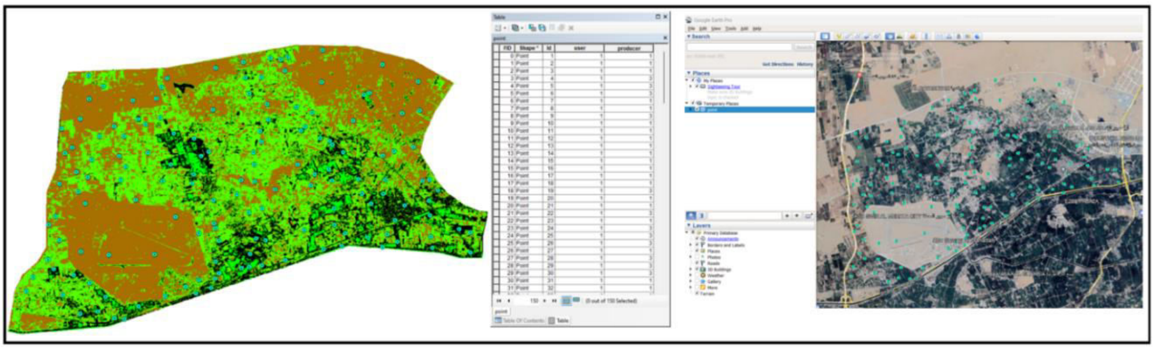

Figure-7. PlanetScope (classified) image of the study area covered with 150 points from random sampling “year, 2016” (Source: Author, 2023).

3.6 Accuracy Assessment Outcomes and Discussion

Different accuracy-assessing parameters were calculated and summarized in Tables 6, 7, and 8 using the formulas provided in section 3.5. According to the findings of the accuracy evaluation, the Artificial Neural Network classifier achieved the highest overall accuracy through the random sampling procedure for the image, with accuracy equal to 77.33 % and 72.00 % for the years 2016 and 2022, respectively. The accuracy of users ranged from 64 % to 100 % in 2016 and from 56 % to 92 % in 2022; whereas the accuracy of producers varied from 68.49 % to 100 % in 2016 and from 60.53 % to 97 % in 2022.The wide range of accuracy suggests that the bare ground class and the other land cover classes are seriously confused. Furthermore, the producer's accuracy measure indicates how accurately the specific category was predicted. The accuracy of the user indicates how trustworthy they believe the classification to be. The more pertinent indicator of the classification's real usefulness in the field is the accuracy of the user. Agriculture was determined to have a higher level of reliability, with user accuracy of 100% in 2016 and 92% in 2022.The overall Kappa coefficient for this study was graded as substantial-moderate, with values of 0.66 for the year 2016 and 0.58 for the year 2022. These customized parameters provide a classifier with additional specific information about the model performance of the specified class or category within our field of interest, in addition to the overall accuracy of classification.

Table-6. Accuracy assessment of the seven classification techniques for two years “2016 and 2022”.

	2016		2022	
	Overall Accuracy (%)	**Kappa Coefficient**	**Overall Accuracy (%)**	**Kappa Coefficient**
Maximum Likelihood	76.00	0.64	69.33	0.54
Minimum Distance	64.67	0.47	54.00	0.31
Mahalanobis Distance	66.67	0.50	66.00	0.49
Spectral Angle Mapper	69.33	0.54	66.00	0.49
Artificial neural network	77.33	0.66	72.00	0.58
K-mean	48.67	0.23	57.33	0.36
ISODATA	63.33	0.45	65.33	0.48

ARPN Journal of Engineering and Applied Sciences

Table-7. Total user and producer accuracy of seven classification techniques for year 2016.

User Accuracy (%)							
LU/LC	**Supervised classification**					**Unsupervised classification**	
	ML	**MD**	**MhD**	**SAM**	**ANN**	**K-means**	**ISODATA**
Bare ground	88	66	78	74	68	52	60
Urban and built-up	44	30	34	44	64	16	38
Agriculture/vegetation	96	98	88	90	100	78	92
Producer Accuracy (%)							
Bare ground	72.13	80.49	69.64	66.07	75.56	65	75
Urban and built-up	88	93.75	100	95.65	100	100	95
Agriculture/vegetation	75	52.69	57.14	63.38	68.49	38.24	51.11

Table-8. Total user and producer accuracy of seven classification techniques for year 2022.

User Accuracy (%)							
LU/LC	**Supervised classification**					**Unsupervised classification**	
	ML	**MD**	**MhD**	**SAM**	**ANN**	**K-means**	**ISODATA**
Bare ground	72	54	70	54	56	52	66
Urban and built-up	54	30	52	60	68	20	30
Agriculture/vegetation	82	78	76	84	92	100	100
Producer Accuracy (%)							
Bare ground	63.16	57.45	62.50	60.00	71.79	83.87	78.57
Urban and built-up	100	88.24	90	93.75	97	76.92	93.75
Agriculture/vegetation	62	45.35	58.46	57.53	60.53	47.17	54.35

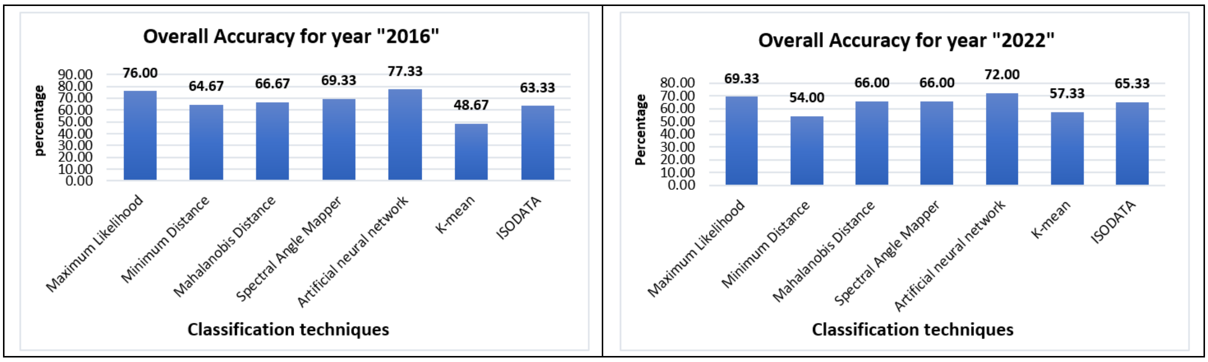

Figure-8. Overall accuracy of seven classification techniques for both year "2016 and 2022" (Source: Author, 2023).

After applying classification accuracy assessment for both years, it was found that Artificial Neural Network classifier has the highest classification accuracy of all of the used classifier. According to ANN classification, agriculture was discovered to be the most prevalent kind of classified land use which covers about 60.48% for 2016 & 53.89% for 2022 of the total study area, Bare ground areas came next, while Built-up areas, which make up 13.61 % in 2016 and 15.80 % in 2022, are the least classified.

3.6.1 Change detection

After classifying the imagery for each date, change detection algorithms were employed to identify

ARPN Journal of Engineering and Applied Sciences

changes in land cover during the period from 2016 to 2022. There are two main types of change detection techniques, which are as follows: pre-classification method and post-classification method. Pre-classification methods examine changes without classifying the image value [43]. On the other hand, the most popular change detection technique today is the post-classification method. Based on a well-categorized classification of land cover, post-classification evaluations of land cover change are done [43]. It has been demonstrated that the most widely used method in change detection analysis is the post classification comparison, so we used PCC in our study.

3.6.2 Post-classification comparison (PCC)

Land use/land cover comparison (LU/LCC) (from-to) data that is detailed is presented in a post-classification comparison, which compares independent classifications from several points in time [44]. For every classification, comparable thematic classes are established, and changes may be observed through a change matrix that shows the quantity of pixels in every class for each of the two time points [44, 45].

In our study, two ANN classified images for both date 2016 and 2022 are used to determine changes in land cover throughout the study period as shown in Figure-8.

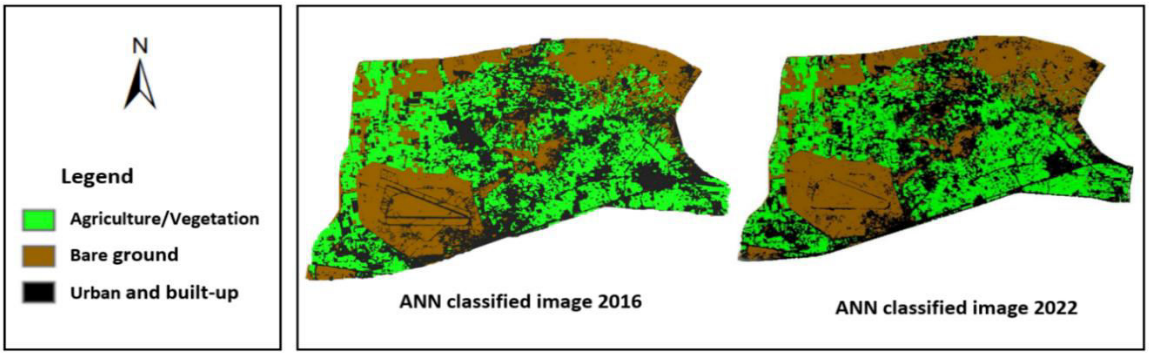

Figure-9. Classified LU/LC thematic images of ABU SUWEIR for years “2016 and 2022” (Source: Author, 2023).

Table-9 and Figure-10 display the annual average change of each class in the study zone in terms of area square kilometer and percentage. The land use practices of the research region have changed during the last six years, from 2016 to 2022, as shown in Table-10 and Figure-11. To help the reader better understand the results, the data acquired is discussed using tables and graphs.

Table-9. Post classification comparison statistics of ABU SUWEIR using ANN.

LU / LC	Date 2016		Date 2022	
	Area (Km^2)	% Total land	Area (Km^2)	% Total land
Bare ground	18.15	25.91	21.23	30.31
Urban and built-up	9.53	13.61	11.07	15.80
Agriculture/vegetation	42.37	60.48	37.75	53.89
Σ	70.05	100.00	70.05	100.00

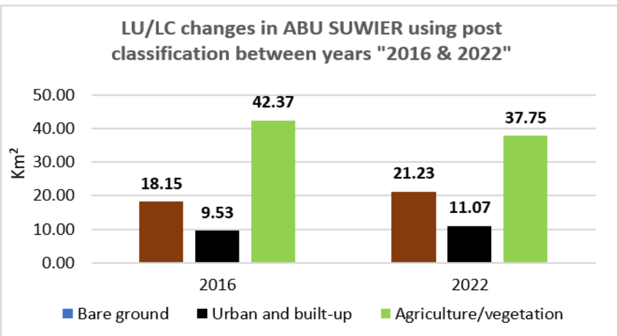

Figure-10. LU/LC changes in ABU SUWIER using post classification comparison between years “2016 and 2022” (Source: Author, 2023).

Table-10. LU/LC changes of ABU SUWEIR using post classification comparison, 2016-2022.

LU/LC	Change between (2022-2016)	
	Change in area (Km^2)	Change (%)
Bare ground	3.08	4.40
Urban and built-up	1.54	2.19
Agriculture/vegetation	-4.62	-6.59
Σ	0.00	0.00

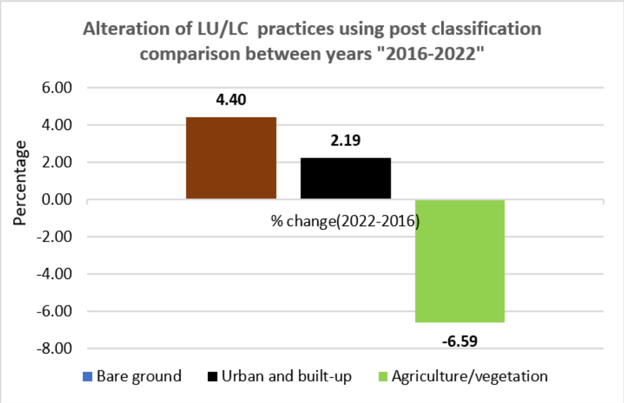

Figure-11. Alteration of LU/LC practices using post classification comparison between years "2016-2022" in percentage (Source: Author, 2023).

Through the analysis of land use patterns, it was discovered that the study area's urbanization pattern was more prevalent across agricultural fields than on the edges of the desert through the period (2016-2022).

4. CONCLUSIONS

The Urban settlements on agricultural land have changed ABU SWAIR, Ismailia's land cover. This research employed multi-temporal, remotely sensed images from 2016 to 2022 to examine this change using multiple methods. Comparing the results to past techniques and digitalization yields the following conclusions:

a) The land use/land cover classification was done through the seven methods. It was found that ANN classifier has the maximum overall accuracy of equal 77.33% for year 2016 and 72.00% for year 2022, with KAPPA coefficient 0.66 and 0.58 for both years respectively. The identified image seems suitable for more investigation as the kappa coefficient is rated from substantial to moderate.

b) The most common type of classified land use, according to ANN classification, is agriculture, which makes up roughly 60.48% of the study area in 2016 and 53.89% in 2022. Bare ground areas are the next most common, with landcover areas equal to 25.91% in 2016 and 30.31% in 2022. Built-up areas, on the other hand, are the least classified, making up 13.61% in 2016 and 15.80% in 2022.

c) The research found that ABU SUWEIR'S land cover patterns changed during the last seven years, with urban and built-up areas increasing by 2.19% and agricultural land declining by 6.59%. Immigration was a persistent factor in this growth. This research highlights the efficacy of remotely sensed data and different GIS techniques for investigating land cover and urban expansion. Urban planners, politicians, and decision-makers may use the newest findings to develop strategic frameworks and policies. It will also help safeguard the city's biological system and solve environmental challenges caused by poor design and inadequate data.

ACKNOWLEDGMENTS

I am pleased to express my sincere gratitude and thanks to the Egyptian Ministry of Planning and Economic Development and those in charge of the National Spatial Data Infrastructure Center (NSDI) (https://mped.gov.eg/) for the cooperation and response I have seen from them, their speed in providing satellite images used in the research, and their support for scientific research and researchers.

REFERENCES

[1] Rahaman S., Kumar P., Chen R., Meadows M. E. and Singh R. B. 2020. Remote Sensing Assessment of the Impact of Land Use and Land Cover Change on the Environment of Barddhaman District, West Bengal, India. Frontiers in Environmental Science, 8. https://doi.org/10.3389/fenvs.2020.00127.

[2] IPCC. 2019. Climate Change and Land: An IPCC Special Report on climate change, desertification, land degradation, sustainable land management, food security, and greenhouse gas fluxes in terrestrial ecosystems. https://www.ipcc.ch/srccl/.

[3] Halder J. C. 2018. Population change and land use dynamics: A case study of Paschim Medinipur District, West Bengal, India. European Journal of Geography, 9(3): 23-44. https://www.eurogeojournal.eu/index.php/egj/article/view/45.

[4] Lambin E. F. and Meyfroidt P. 2011. Global land use change, economic globalization, and the looming land scarcity. Proceedings of the National Academy of Sciences of the United States of America (PNAS), 108(9): 3465-3472. https://doi.org/10.1073/pnas.1100480108.

[5] Jarah S. H. A., Zhou B., Abdullah R. J., Lu Y. and Yu W. 2019. Urbanization and urban sprawl issues in city structure: A case of the Sulaymaniah Iraqi Kurdistan Region. Sustainability, 11(2): 485. https://doi.org/10.3390/su11020485.

[6] Huang S., Tang L., Hupy J. P., Wang Y. and Shao G. 2021. A commentary review on the use of normalized difference vegetation index (NDVI) in the era of popular remote sensing. Journal of Forestry Research, 32(1): 1-6. https://doi.org/10.1007/s11676-020-01155-1.

[7] Shalaby A. and Moghanm F. S. 2015. Assessment of urban sprawl on agricultural soil of northern Nile Delta of Egypt using RS and GIS. Chinese Geographical Science, 25, 274-282. 10.1007/s11769-015-0748-z.

[8] Shaw R. and Das A. 2018. Identifying peri-urban growth in small and medium towns using GIS and remote sensing technique: A case study of English Bazar Urban Agglomeration, West Bengal, India. The Egyptian Journal of Remote Sensing and Space Science, 21(2): 159-172. https://doi.org/10.1016/j.ejrs.2017.01.002.

[9] Toure S. I., Stow D. A., Shih H. C., Weeks J. and Lopez-Carr D. 2018. Land cover and land use change analysis using multi-spatial resolution data and object-based image analysis. Remote Sensing of Environment, 210, 259-268. https://doi.org/10.1016/j.rse.2018.03.023.

[10] Mosammam H. M., Nia J. T., Khani H., Teymouri A. and Kazemi M. 2017. Monitoring land use change and measuring urban sprawl based on its spatial forms: The case of Qom city. Egyptian Journal of Remote Sensing and Space Science, 20(1): 103-116. https://doi.org/10.1016/j.ejrs.2016.08.002.

[11] Yang X. and Liu Z. 2005. Use of satellite-derived landscape imperviousness index to characterize urban spatial growth. Computers, Environment and Urban Systems, 29(5): 524-540. https://doi.org/10.1016/j.compenvurbsys.2005.01.005.

[12] Keshtkar H., Voigt W. and Alizadeh E. 2017. Land-cover classification and analysis of change using machine-learning classifiers and multi-temporal remote sensing imagery. Arabian Journal of Geosciences, 10, 1-15. https://doi.org/10.1007/s12517-017-2899-y.

[13] An Y., Tsou J. Y., Wong K., Zhang Y., Liu D. and Li Y. 2018. Detecting land use changes in a rapidly developing city during 1990-2017 using satellite imagery: A case study in Hangzhou Urban area, China. Sustainability, 10(9): 3303. https://doi.org/10.3390/su10093303.

[14] Khandve, P. V., and Mokadam, A. M. (2011). Application of GIS in Environmental Engineering. National Conference on Environment Pollution and Management, 244-250. https://www.researchgate.net/publication/292695439_Application_of_GIS_in_Environmental_Engineering.

[15] Omusotsi O. G. 2019. Role of GIS as a Tool for Environmental Planning and Management. International Journal of Research in Environmental Science (IJRES), 5(1). https://doi.org/10.20431/2454-9444.0501002.

[16] Abeed R., Clerbaux C., Clarisse L., Damme M. Van, Coheur P. F. and Safieddine S. 2021. A space view of agricultural and industrial changes during the Syrian civil war. Elementa: Science of the Anthropocene, 9(1): 1-13. https://doi.org/10.1525/elementa.2021.000041.

[17] Kulo N. 2018. Benefits of the Remote Sensing Data Integration. 1st Western Balkan Conference on GIS, Mine Surveying, Geodesy and Geomatic, 0-14. https://www.researchgate.net/publication/329443299_Benefits_of_the_Remote_Sensing_Data_Integration.

[18] Chander G., Markham B. L. and Helder D. L. 2009. Summary of current radiometric calibration coefficients for Landsat MSS, TM, ETM+, and EO-1 ALI sensors. Remote sensing of environment, 113(5), 893-903. https://doi.org/10.1016/j.rse.2009.01.007.

[19] Mohsen A., Elshemy M. and Zeidan B. A. 2018. Change detection for Lake Burullus, Egypt using remote sensing and GIS approaches. Environmental Science and Pollution Research, 25, 30763-30771. 10.1007/s11356-016-8167-y.

[20] United States Geological Survey (USGS) U.S. Department of the Interior U.S. Geological Survey. https://www.usgs.gov/landsat-missions/using-usgs-landsat-level-1-data-product. Accessed 15 August 2015.

[21] Ahmed S. 2021. Comparison of satellite images classification techniques using landsat-8 data for land cover extraction. International Journal of Intelligent Computing and Information Sciences, 21(3): 29-43. 10.21608/ijicis.2021.78853.1098.

[22] Chavez Jr P. S. 1989. Radiometric calibration of Landsat Thematic Mapper multispectral images. Photogrammetric engineering and remote sensing. 55(9): 1285-1294.

[23] Eastman J. R. 1999. Guide to GIS and Image processing. Clark Labs, Clark University 950 Main Street Worcester, MA. https://www.researchgate.net/publication/242377547_Guide_to_GIS_and_Image_Processing_Volume_2.

[24] Mohamed B. M. 2012. Modelling of urban sprawl in Austin, Texas area using Landsat imagery. (M.S. Thesis). Murray State University, Kentucky.

[25] Singh A. 1989. Review article digital change detection techniques using remotely-sensed data. International journal of remote sensing, 10(6): 989-1003. https://doi.org/10.1080/01431168908903939.

[26] Alamri S. S. A., Bin-Sama A. S. A., Bin-Habtoor A. S. Y. 2016. Satellite Image Classification by Using Distance Metric. International Journal of Computer Science and Information Security (IJCSIS). 14(3).

[27] Sathya P. and Deepa V. B. 2017. Analysis of Supervised Image Classification Method for Satellite Images. International Journal of Computer Science Research (IJCSR). 5(2): 16-19.

[28] Prasad S. V. S., Savithri T. S. and Krishna I. V. M. 2015. Techniques in image classification; A survey. Global Journal of Researches in Engineering: Electrical and Electronics Engineering, 15(6): 17-32. https://engineeringresearch.org/index.php/GJRE/article/view/1307.

[29] Jensen J. R. 2005. Digital image processing: a remote sensing perspective. Upper Saddle River, NJ: Prentice Hall.

[30] Kuching S. 2007. The performance of maximum likelihood, spectral angle mapper, neural network and decision tree classifiers in hyperspectral image analysis. Journal of Computer Science, 3(6): 419-423. https://doi.org/10.3844/jcssp.2007.419.423.

[31] Richards J. A. 1999. Remote Sensing Digital Image Analysis BerlinSpringer-Verlag240. https://doi.org/10.1007/978-3-662-03978-6.

[32] McCloy K. R. 2005. Resource management information systems: Remote sensing, GIS and modelling. CRC Press. https://doi.org/10.1201/b17305

[33] Nath S. S., Mishra G., Kar J., Chakraborty S. and Dey N. 2014, July. A survey of image classification methods and techniques. In 2014 International conference on control, instrumentation, communication and computational technologies (ICCICCT) (pp. 554-557). IEEE. 10.1109/ICCICCT.2014.6993023

[34] Rao V. B. and Rao H. V. 1995. C++, neural networks and fuzzy logic. Mis: Press.

[35] RV A. and SV R. 2020. Unsupervised ISODATA algorithm classification used in the Landsat image for predicting the expansion of Salem urban, Tamil Nadu. Indian J. Sci. Technol, 13, 1619-1629. 10.17485/IJST/v13i16.271

[36] Morissette L. and Chartier S. 2013. The k-means clustering technique: General considerations and implementation in Mathematica. Tutorials in Quantitative Methods for Psychology, 9(1): 15-24. https://doi.org/10.20982/tqmp.09.1.p015

[37] Chaikaew P. 2019. Land Use Change Monitoring and Modelling using GIS and Remote Sensing Data for Watershed Scale in Thailand. In L. C. Loures (Ed.), Land Use - Assessing the Past, Envisioning the Future (pp. 165-181). IntechOpen. https://doi.org/10.5772/intechopen.79167

[38] Mohajane M., Essahlaoui A., Oudija F., Hafyani M. El, Hmaidi A. El, Ouali A. El, Randazzo G. and Teodoro A. C. 2018. Land use/land cover (LULC) using landsat data series (MSS, TM, ETM+ and OLI) in azrou forest, in the central middle atlas of Morocco. Environments, 5(12): 1-16. https://doi.org/10.3390/environments5120131

[39] Rwanga S. S. and Ndambuki J. M. 2017. Accuracy assessment of land use/land cover classification using remote sensing and GIS. International Journal of Geosciences. 8(04): 611.

[40] Abd El Aal A. K., Kamel M. and Alyami S. H. 2020. Environmental analysis of land use and land change of Najran city: GIS and remote sensing. Arabian journal for science and engineering. 45, 8803-8816.

[41] Parraga-Alavaa J., Alcivar-Cevallos R., Vaca-Cardenas L., Meza J. 2021. UrbangEnCy: An emergency events dataset based on citizen sensors for monitoring urban scenarios in Ecuador. Data in Brief, 34, 106693, https://doi.org/10.1016/j.dib.2020.106693

[42] Landis J. R. and Koch G. G. 1977. A One-Way Components of Variance Model for Categorical Data. Biometrics. 33, 671-679. https://doi.org/10.2307/2529465.

[43] Haque M. I. and Basak R. 2017. Land cover change detection using GIS and remote sensing techniques: A spatio-temporal study on Tanguar Haor, Sunamganj,

Bangladesh. The Egyptian Journal of Remote Sensing and Space Science, 20(2): 251-263. https://doi.org/10.1016/j.ejrs.2016.12.003

[44] Morgan G. R. and Hodgson M. E. 2021. A Post-Classification Change Detection Model with Confidences in High Resolution Multi-Date sUAS Imagery in Coastal South Carolina. International Journal of Remote Sensing, 42(11): 4309-4336. https://doi.org/10.1080/01431161.2021.1890266

[45] Attri P., Chaudhry S. and Sharma S. 2015. Remote Sensing & GIS based Approaches for LULC Change Detection-A Review. International Journal of Current Engineering and Technology, 5(5): 3126-3137. https://www.researchgate.net/publication/325145097_Remote_Sensing_GIS_based_Approaches_for_LULC_Change_Detection_-_A_Review